Investigations of the Stability of GaAs for Photoelectrochemical H2 Evolution in Acidic or Alkaline Aqueous Electrolytes

Journal:	*Journal of Materials Chemistry A*
Manuscript ID	TA-ART-05-2021-004145.R1
Article Type:	Paper
Date Submitted by the Author:	30-Aug-2021
Complete List of Authors:	Yu, Weilai; California Institute of Technology, Division of Chemistry and Chemical Engineering Richter, Matthias; California Institute of Technology, Joint Center for Artificial Photosynthesis Simonoff, Ethan; California Institute of Technology, Chemistry Brunschwig, Bruce; California Institute of Technology , Beckman Institute Lewis, Nathan S.; California Institute of Technology, Chemistry and Chemical Engineering

Investigations of the Stability of GaAs for Photoelectrochemical H_2 Evolution in Acidic or Alkaline Aqueous Electrolytes

Weilai Yu[1], Matthias Richter[1], Ethan Simonoff[1], Bruce S. Brunschwig[*2] and Nathan S. Lewis[*1,2]

[1] Division of Chemistry and Chemical Engineering and [2] Beckman Institute, California Institute of Technology, Pasadena CA, 91125

Email: nslewis@caltech.edu, bsb@caltech.edu

Abstract

The long-term stability of p-GaAs photocathodes has been investigated for the hydrogen-evolution reaction (HER) in contact with either 1.0 M H_2SO_4(aq) or 1.0 M KOH(aq). Stability for the HER was evaluated using p-GaAs electrodes that were either etched or coated with active HER catalysts (Pt and CoP). Changes in surface characteristics of GaAs after exposure to electrochemical conditions were monitored by X-ray photoelectron spectroscopy (XPS), and electrode dissolution processes were evaluated by inductively coupled plasma mass spectrometry (ICP-MS). Consistent with thermodynamic predictions, after operation of the HER at pH 0 or pH 14, illuminated etched p-GaAs electrodes exhibited minimal dissolution while preserving a nearly stoichiometric surface. Electrodeposition or sputtering of Pt on the p-GaAs surface promoted the formation of excess As^0 via an interfacial reaction during the HER. The resulting non-stoichiometric As^0-rich surface of p-GaAs/Pt electrodes caused a loss in photoactivity as well as substantial cathodic dark current. In contrast, p-GaAs electrodes coated with thin-film CoP catalysts did not display an increase in surficial As^0 after operation of the HER in acidic electrolytes. Minimization of deleterious interfacial reactions is thus critical to obtain extended stability in conjunction with high performance from p-GaAs photocathodes.

Introduction

Photoelectrochemical (PEC) water-splitting devices, using light-absorbing semiconductors and fuel-forming catalysts, offer a one-step conversion of sunlight and water to hydrogen and oxygen.[1–3] However, strongly acidic or alkaline electrolytes are required to prevent the formation of pH gradients that reduce the energy-conversion efficiency of such devices.[4] This requirement presents substantial challenges to the long-term operation and materials stability of suitable semiconductors, catalysts, and membranes.

Extensive research efforts have been devoted to improving the stability of PEC devices. Protective and/or catalytic coatings on semiconductors have shown promise for mitigation of photoelectrode degradation.[5–7] In a few cases, photoelectrode lifetimes of a few hundred hours have been achieved,[8–10] but further advances are required to extend device lifetimes to years or decades. A fundamental understanding of the corrosion mechanisms of semiconductors under operating conditions will underpin rational strategies to obtain long-term stability of photoelectrodes. For solar-driven water-splitting devices, overpotentials (η) of $\geq$100 mV and $\geq$350 mV are required to drive the hydrogen- and oxygen-evolution half-reactions (HER/OER), respectively, at current densities (J) of 10 mA cm^{-2}.[11] Hence, the stability and corrosion pathways of semiconductors should be primarily evaluated for photocathodes and photoanode at potentials (E) $\leq$ -0.1 V and $\geq$ 1.58 V vs. the reversible hydrogen electrode (RHE), respectively.[12] Moreover, combining experimental investigations of semiconductor stability with the Pourbaix diagram (**Figure S1**) for a material of interest can reveal both the thermodynamics and kinetics of corrosion processes.

A tandem solar-driven water-splitting device uses a combination of large and small band-gap semiconductors.[13] Due to its relatively small 1.42 eV band gap, gallium arsenide (GaAs) is a promising light-absorber for solar-fuel devices. However, n-type GaAs (n-GaAs) photoanodes rapidly corrode under potentials needed to effect the OER, limiting the stability of such systems in aqueous electrolytes.[14,15] Oxidative corrosion of GaAs is promoted by the migration of photogenerated holes (h^+) to the GaAs/H_2O interface, resulting in the oxidation of As^{3-} anions as well as the irreversible dissolution of GaAs. The electrochemical characteristics of this anodic corrosion process, together with the associated surface transformation, have been extensively studied in strongly acidic or alkaline electrolytes.[16–22] Under certain conditions, n-GaAs photoanodes passivate by forming As^0 and AsO_x as well as non-stoichiometric surfaces. Oxidants such as Fe^{3+} and Br_2 accelerate the kinetics of anodic etching (**Eq 1**) of GaAs via a galvanic pathway, enabling the development of electrochemical nanoimprint lithography to fabricate anisotropic nanostructures of GaAs.[22–25]

$$GaAs(s) + 10OH^-(aq) \rightarrow GaO_3^{3-}(aq) + AsO_2^-(aq) + 6e^- + 5H_2O(l) \text{ (in alkaline electrolyte)} \quad (1)$$

Other redox couples such as Se_2^{2-}/Se^{2-} inhibit the anodic corrosion of GaAs by kinetic competition for photogenerated holes.[26–28] To physically mitigate the anodic corrosion of GaAs, surface passivation layers, including amorphous TiO_2 (a-TiO_2) or single-layer graphene, can yield sustained operation of GaAs photoanodes over extended time periods.[15,29] Planar np^+-GaAs photoanodes protected by a-TiO_2 have shown long-term stability for the OER (> 25 h) in 1.0 M KOH(aq),[15] while producing a photovoltage of 0.81 V and a photocurrent density of 14.3 mA cm^{-2} under simulated 1-sun illumination.[15] In contact with the $FeCp_2^{+/0}$ redox couple, single crystalline planar GaAs photoanodes exhibit a photovoltage of > 0.7 V and a photocurrent density of > 16 mA cm^{-2} under a simulated solar intensity of 65 mW cm^{-2}, resulting in 10 % ideal regenerative cell energy conversion efficiencies.[30] In the same electrolyte, n-GaAs nanowire array photoanodes exhibit a photovoltage of 0.59 V and a photocurrent density of 24.6 mA cm^{-2}, providing an energy-conversion efficiency of >8 % under 1-sun illumination.[28] Chemically modified single-crystal n-GaAs photoanodes in contact with 1.0 M KOH(aq) containing the $Se^{-/2-}$ redox couple have moreover exhibited >16 % energy conversion efficiencies.[31,32] Related III-V tandem cells have exhibited solar-to-hydrogen energy conversion efficiencies of >19%, although these efficiencies only persist for a time scale of hours in the laboratory.[14,33]

In contrast, the long-term stability of p-type GaAs (p-GaAs) photocathodes is not well established for performing the HER in either acidic or alkaline aqueous electrolytes. Early work revealed Fermi level pinning for p-GaAs electrodes in contact with various redox couples, limiting the PEC performance.[34,35] Recently, extended stability (96 h) has been reported for unmodified GaAs photocathodes performing the HER, with minimal surface etching in 3.0 M H_2SO_4(aq).[36] This report is in contrast to the general perception that III-V semiconductors will inevitably rapidly corrode in strongly acidic or alkaline aqueous electrolytes.[14,33,37] Regardless of stability, etched p-GaAs photocathodes in this work displayed low onset potentials (< 0 V vs. RHE) for the HER, and a E of ~-0.3 V vs. RHE was required to produce a current density of -15 mA cm^{-2}.[36] Overcoming the high η for the HER at a GaAs surface requires active HER catalysts such as Pt or CoP.[38] By accelerating the surface kinetics, the HER catalysts may also influence the corrosion pathway of p-GaAs photocathodes through modification of the surface potential during operation as a photocathode.[12]

Herein, we present a systematic study of the stability of p-GaAs photocathodes for the HER in either 1.0 M H_2SO_4(aq) or 1.0 M KOH(aq), with or without HER catalysts (Pt or CoP). Our experimental approach consists of: (1) long-term chronoamperometry (CA) experiments on GaAs electrodes in an oxygen-free environment, (2) measurement of the concentrations of dissolved Ga and As ions in the electrolyte by ICP-MS during CA, and (3) characterization of the GaAs surface by X-ray photoelectron spectroscopy (XPS). An air-free sample transport method between the electrochemical and XPS measurements was used to minimize oxidation by ambient air. The behavior of n-GaAs electrodes maintained at -0.1 V vs. RHE in the dark was compared with the behavior of illuminated p-GaAs electrodes evaluated under cathodic current flow. Changes in the surface characteristics of p-GaAs electrodes after electrochemical measurements were correlated with the evolution of the current density vs. potential *(J-E)* behavior. This work provides fundamental insights into both the physical and electrochemical stability of p-GaAs photocathodes for the HER, as well as insight into the interfacial interactions between GaAs and various HER catalysts that can affect both the stability and PEC performance of the resulting photocathodes.

Experimental

Materials

Full experimental details are available in the supporting information. Single-side polished Si doped n-GaAs(100) (with a doping density, $N_d = 1\text{-}5\times10^{17}$ cm^{-3}), and Zn-doped p-GaAs(100) ($N_d=1\text{-}5\times10^{17}$ cm^{-3}) wafers were purchased from AXT Inc. Ohmic contact to n-GaAs was made by evaporating In metal followed by annealing (forming gas, 400 ºC, 10 min), whereas sputtering Ni metal produced an ohmic contact to p-GaAs.[15] Prior to electrochemical measurements, GaAs electrodes were etched in

0.04 % (by volume) Br_2/CH_3OH for 30 s, then in 1.0 M KOH(aq) for 15 s, rinsed with methanol, and blown dry under a stream of N_2(g). Electrochemical measurements were performed in a nitrogen-filled glove box (O_2 concentration <0.3 ppm). The CA experiments were performed using a two-compartment compression cell with an ion-exchange membrane. The catholyte was continually purged with H_2(g), and separate outlets were provided for H_2(g) and O_2(g). During CA, *J-E* data were periodically measured after 15 s at open-circuit. No IR compensation was used. A 150 W halogen bulb with a fiber optic was used as the illumination source and was calibrated to provide 1 sun (100 mW cm^{-2}) of intensity at the electrode surface. Pt from an aqueous solution of 5 mM K_2PtCl_4/0.5 M KCl was electrodeposited on illuminated p-GaAs electrodes until a fixed charge density had passed. Electrodeposition of CoP on illuminated p-GaAs electrodes followed a published procedure.[38] Sputter deposition of Pt on p-GaAs was performed under an Ar atmosphere. Before catalyst deposition, all GaAs samples were freshly etched and dried.

Analytical Methods

During CA, 0.2 mL aliquots of solution were withdrawn from the catholyte and replaced with fresh electrolyte. The electrolytes samples were subsequently analyzed by inductively coupled plasma mass spectrometry (ICP-MS). Calibration solutions were prepared by dilution of multi-element standard solutions. The total amounts of Ga or As ions dissolving from GaAs were normalized to the geometric electrode area and then converted to the equivalent corrosion thickness in nm of GaAs.

X-ray photoelectron spectroscopy (XPS) was performed using a Kratos Axis Ultra system with an Al Kα X-ray source, with a base pressure of ~5 $\times 10^{-9}$ Torr. After CA, electrodes were rinsed with deionized water and blown dry under a stream of N_2(g) in the glove box. In the N_2-filled glove box, samples were loaded into a suitcase for air-free transport to the XPS instrument. XPS peak fitting was performed using CasaXPS software version 2.3.18. Binding energies from the original spectra were referenced to the adventitious carbon peak at 284.8 eV. Spectra were fitted after a Shirley background had been subtracted. Fitting of the As 3d and the Ga 3d XP spectra used Voigt-functions constrained to an area ratio of 3:2 in addition to constraining each of the spin-orbit components of the signal to having mutually identical peak widths. The Ga 2p peaks were fit using an asymmetric Lorentzian function, whereas other peaks were fit with a Voigt function.

Scanning-electron microscopy (SEM) images were obtained using a Nova NanoSEM 450 (FEI). Transmission-electron microscopy (TEM) cross-sections were prepared using a focused Ga ion beam (FIB). TEM images were obtained using a FEI Osiris at an accelerating voltage of 200 kV equipped with a Gatan 2K TEM camera and a Bruker Energy Dispersive X-ray Spectroscopy (EDS) instrument. Atomic-force microscopy (AFM) images were obtained on a Bruker Dimension Icon using Bruker ScanAsyst-Air probes.

Results

Stability of GaAs electrodes at open-circuit potential (E_{oc}) in the dark

The dissolution rates in 1.0 M H_2SO_4(aq) or 1.0 M KOH(aq) of n- and p-GaAs(100) electrodes at the open-circuit potential (E_{oc}) in the dark were measured in a N_2-filled glove box (**Figure 1 and Figure S2)**. After an initial drift, the E_{oc} values stabilized for >20 h between +0.1 and +0.5 V vs. RHE. In acidic electrolytes, dissolution of Ga and As ions was observed initially **(Figure S3)**. The concentrations of dissolved Ga and As ions in the electrolyte linearly increased with time. After the initial dissolution, the measured corrosion rates were similar for Ga and As ions, indicating stoichiometric dissolution of GaAs at E_{oc} in the dark. The corrosion rates of n- and p-GaAs in 1.0 M H_2SO_4(aq) were ~0.7 and 0.2 nm h^{-1}, respectively, whereas in 1.0 M KOH(aq) the rates were ~6 and 7 nm h^{-1}, respectively **(Table S1)**.

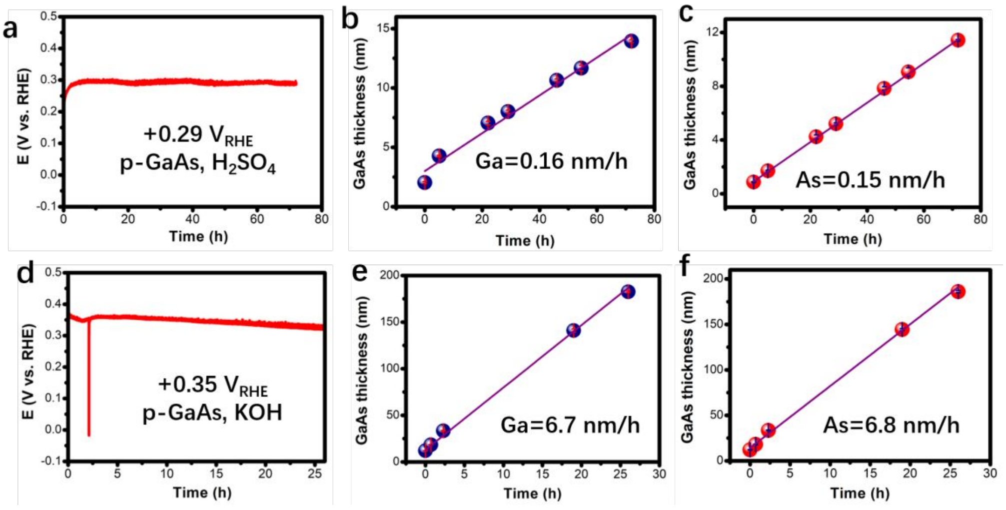

Figure 1. Corrosion rates of p-GaAs at the open-circuit potential (E_{oc}) in the dark. Comparison of

(a,d) the measured E_{oc} values versus time in the dark, and the corrosion thickness of GaAs based on the concentrations of (b,e) Ga ions and (c,f) As ions in (a-c) 1.0 M H_2SO_4(aq) and (d-f) 1.0 M KOH(aq).

Stability of n-GaAs electrodes at -0.1 V vs. RHE in the dark

During CA at E = -0.1 V vs. RHE in the dark, $|J|$ of n-GaAs(100) electrodes remained low in either 1.0 M H_2SO_4(aq) or 1.0 M KOH(aq). In 1.0 M H_2SO_4(aq), $|J|$ initially decreased and was ~0.014 mA cm^{-2} in the first 10 h (**Figure S4a)**. Small, abrupt increases in $|J|$ were then observed every few hours, with $|J|$ gradually increasing to 0.026 mA cm^{-2} after 30 h. The calculated corrosion thickness of n-GaAs, based on the amount of dissolved Ga ions, rose from ~0.86 to 1.25 nm after 35 h. However, the As concentration in the electrolyte did not increase over time (**Figure S4b**). After CA, approximately 3 times more Ga than As was detected in the acidic electrolyte. In 1.0 M KOH(aq), $|J|$ was initially ~0.005 mA cm^{-2}, then decreased to <0.003 mA cm^{-2} and remained stable for the subsequent 30 h (**Figure S4a)**. The dissolved Ga and As ions increased slightly during the first 10 h but remained constant afterwards, accounting for <1 nm in GaAs thickness (**Figure S4c**).

For all n-GaAs samples before and after CA, the XPS data in the Ga $2p_{3/2}$ region exhibited a single peak at a binding energy (BE) of 1116.9 ± 0.1 eV, attributable to the Ga^{3+} cations of GaAs (**Figure S4d**). The As 3d XP spectrum of an n-GaAs sample before CA was well-fit with two doublets, with the larger As $3d_{5/2}$ peak at BE = 40.8 eV assigned to the As^{3-} anions of GaAs, and the minor peak at BE = 41.3 eV assigned to surficial As^0 (**Figure S4e**). This peak assignment is based upon previous XPS studies of GaAs surface.[39–41] Before CA, the As^0/As ratio was 0.22±0.02, whereas after CA this ratio increased to 0.41±0.01 in 1.0 M H_2SO_4(aq), and but decreased to 0.11±0.02 in 1.0 M KOH(aq). Scanning-electron microscopy (SEM) images of n-GaAs samples revealed negligible changes in surface morphology after CA in either 1.0 M H_2SO_4(aq) or 1.0 M KOH(aq) (**Figure S5a-c**). Some small particles visible on the sample surface are likely derived from pre-existing impurities, which were observed before CA. Atomic-force microscopy (AFM) images showed that after CA in either electrolyte the surface roughness remained at ~0.4 nm in flat regions of the n-GaAs electrodes (**Figure S5d-f**).

Stability of etched p-GaAs electrodes under cathodic current flow with simulated 1-sun illumination

The stability of etched p-GaAs(100) electrodes was also evaluated at E = -0.2 or -0.6 V vs. RHE in 1.0 M H_2SO_4(aq) under simulated 1-sun illumination (**Figure 2a&2d**). The variation in J during CA was due to the formation and release of H_2 bubbles.[42,43] During CA at -0.2 V vs. RHE, $|J|$ decreased in the first 2 h from ~11 to 3 mA cm^{-2} and then remained stable (**Figure 2a**). The decrease in $|J|$ is consistent with an initial negative shift in the J-E behavior of the illuminated p-GaAs electrode (**Figure 2b**). After 20 h, the potential required to produce 10 mA cm^{-2} of cathodic current density (E_{10}) shifted from -0.14 V to -0.26 V vs. RHE. The measured J-E behavior of etched p-GaAs photoelectrodes is comparable that described in other recent reports.[36,44–47] At -0.6 V vs. RHE, the maximum $|J|$ of a p-GaAs photoelectrode was stable at ~20 mA cm^{-2} (**Figure 2d**). An analogous negative shift in the J-E behavior was observed, and after 65 h E_{10} shifted from -0.17 V to -0.41 V vs. RHE (**Figure 2e**).

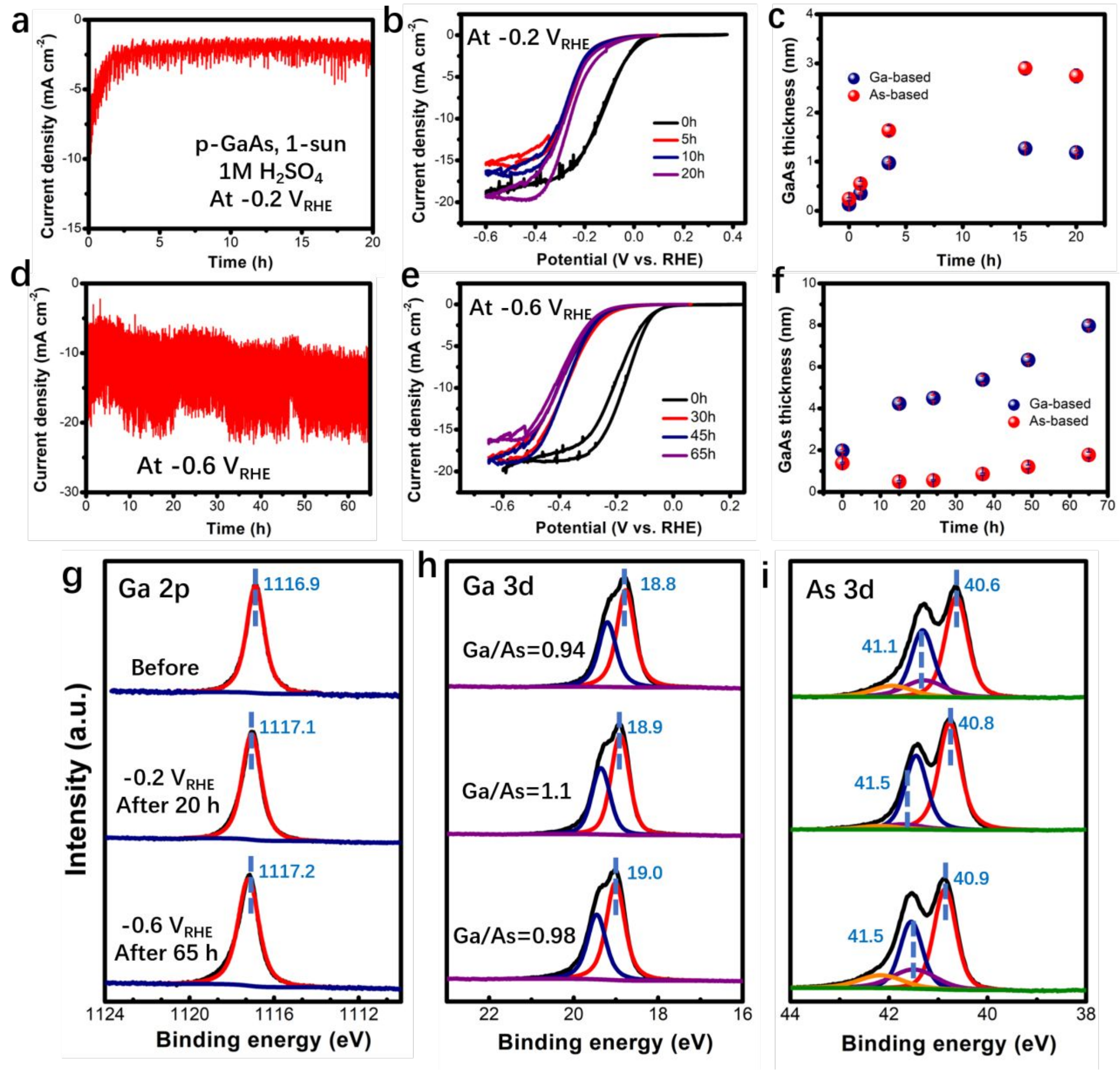

Figure 2. Results of etched p-GaAs photoelectrodes evaluated in acidic electrolytes. (a,d) CA of p-GaAs electrodes at (a) -0.2 V and (d) -0.6 V vs. RHE in 1.0 M H_2SO_4(aq) under simulated 1-sun illumination. (b,e) Comparison of the *J-E* behavior of illuminated p-GaAs electrodes periodically measured over time during CA at (b) -0.2 V vs. RHE for 20 h and (e) -0.6 V vs. RHE for 65 h. Scan rates: 50 mV s^{-1}. (c,f) Corrosion thickness (nm) of p-GaAs versus time for the p-GaAs electrodes during CA in (a,d) determined by the concentrations of dissolved Ga and As ions in the electrolytes. (g-i) Comparison of XP spectra in the (g) Ga $2p_{3/2}$, (h) Ga 3d and (i) As 3d regions for p-GaAs electrodes before and after CA in (a,d).

In 1.0 M H_2SO_4(aq), the concentrations of Ga ions in the electrolyte increased linearly with time, resulting in calculated corrosion rates of 0.12 and 0.09 nm h^{-1} for p-GaAs electrodes at E = -0.2 V and -0.6 V vs. RHE, respectively (**Figure 2c&f**). However, the As concentrations remained low and did not increase with time. After both CA experiments, the Ga 3d XPS data showed negligible changes in the surface stoichiometry of p-GaAs (**Figure 2g-i**). The As^0/As ratio for an etched p-GaAs sample before CA was 0.22±0.05. The ratio changed slightly to 0.13±0.04 and 0.28±0.03, after CA at E = -0.2 V vs. RHE and at E = -0.6 V vs. RHE, respectively. For both samples, Ga/As ratios of ~1 indicated that the surface of p-GaAs electrodes remained nearly stoichiometric after effecting the HER. SEM and AFM images showed that after CA the surface of both p-GaAs electrodes remained generally flat (**Figure S6**).

During CA at -0.6 V vs. RHE in 1.0 M KOH(aq), an etched p-GaAs electrode exhibited a stable $|J|$ of ~20 mA cm^{-2} for 46 h under simulated 1-sun illumination (**Figure 3a**). Within the first 5 h of CA, the p-GaAs electrode exhibited negligible J in the dark, but after 20 h J in the dark increased to ~7.4 mA cm^{-2}. The increase in $|J|$ in the dark correlated with changes over time in the J-E behavior of the illuminated p-GaAs electrode (**Figure 3b**). After 46 h of CA, a comparison of the J-E behavior in the dark to the J-E behavior under illumination showed that the electrode photoactivity was preserved despite the substantial dark current density (**Figure S7**). ICP-MS analysis of the sampled electrolytes revealed a dissolution of ~1 nm GaAs during the initial 10 h of CA, but no further dissolution was observed (**Figure 3c**).

Under illumination, a second p-GaAs electrode exhibited a gradually decreasing $|J|$ during the 4 h CA at E = -0.6 V vs. RHE in 1.0 M KOH(aq) (**Figure S8**). After a short pause (15 s) at E_{oc}, followed by three CV cycles, the current density returned to its original value (**Figure S8a**). The J-E behavior under illumination remained nearly constant over 4 h, but the dark J increased markedly (**Figure S8b-c**).

SEM images showed that the surfaces of both p-GaAs samples evaluated in 1.0 M KOH(aq) remained flat, whereas AFM images revealed distinct nano-sized particles (**Figure S9)**. After CA, XPS analysis (**Figure 3d-f**) indicated similar surface conditions for both samples, with no evidence for formation of new species. The Ga/As ratios of the p-GaAs electrodes slightly increased to ~1.4 and 1.1 after the 4 h and 46 h CA, respectively. The As^0/As ratios were 0.17±0.03 and 0.13±0.04 after the 4 h and 46 h CA, respectively.

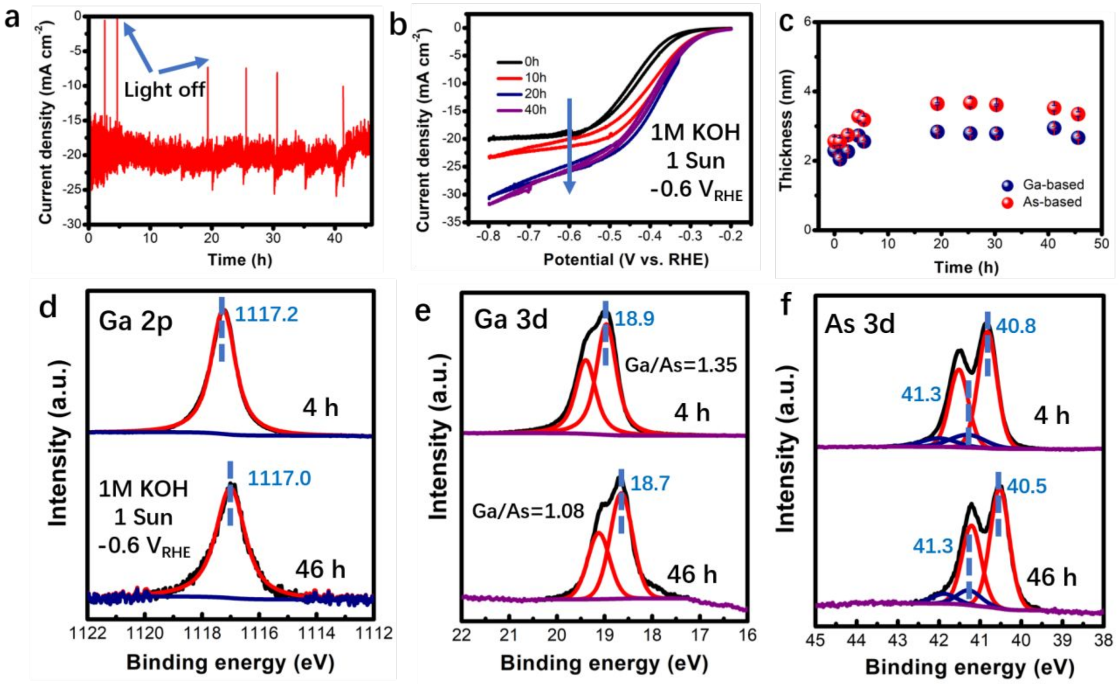

Figure 3. Results of etched p-GaAs photoelectrodes evaluated in alkaline electrolytes. (a) CA of a p-GaAs electrode at -0.6 V vs. RHE in 1.0 M KOH(aq) under simulated 1-sun illumination; the inset arrows represent the times when light was turned off. (b) *J-E* behavior of an etched p-GaAs electrode under simulated 1-sun illumination during CA in (a). (c) Corrosion thickness (nm) of a p-GaAs electrode versus time during CA in (a) determined by the concentrations of dissolved Ga and As ions in the electrolyte. (d-f) Comparison of XP spectra in the (d) Ga $2p_{3/2}$, (e) Ga 3d, (f) As 3d regions for two different p-GaAs electrodes held at -0.6 V vs. RHE for 4 h and 46 h, respectively.

Preparation and characterization of p-GaAs/Pt_{ed} electrodes.

Pt was electrodeposited on the surface of illuminated p-GaAs, producing p-GaAs/$Pt_{ed}(x)$ electrodes with estimated thicknesses of x = 0.5 nm or x = 5 nm of Pt. SEM and AFM images (**Figure S10)** revealed that both of the as-prepared p-GaAs/Pt_{ed}(0.5) and p-GaAs/Pt_{ed}(5) samples displayed a nanoparticulate morphology that moreover exhibited an increase in surface roughness (R_q) relative to the samples without a Pt deposit. For an as-prepared p-GaAs/Pt_{ed}(0.5) electrode, the Ga 3d XPS data showed the Ga^{3+} cations of GaAs at BE = 18.9 eV as well as GaO_x at a BE = 20.7 eV (**Figure S11**). The XP spectrum of the As 3d region revealed the As^{3-} anions of GaAs at BE = 40.8 eV, as well as signals for As^0 at BE = 41.3 and AsO_x at BE = 44.0 eV (**Figure S11**). The oxides of As and Ga likely formed during the Pt electrodeposition. Moreover, the as-prepared p-GaAs/Pt_{ed}(0.5) exhibited a nearly stoichiometric surface (Ga/As=1.1) with an As^0/As ratio of 0.36±0.06 (**Figure S11**).

Stability of p-GaAs/Pt_{ed}(0.5) electrodes at -0.2 V vs. RHE under simulated 1-sun illumination

The stability of a p-GaAs/Pt_{ed}(0.5) electrode was evaluated at E = -0.2 V vs. RHE in 1.0 M H_2SO_4(aq) (**Figure 4**). The first three *J-E* cycles under illumination showed a light-limited J (J_{ph}) of ~ -16 mA cm^{-2} (**Figure S12a**). Within the first 30 min of CA, $|J|$ rapidly increased from 10 to 40 mA cm^{-2}, and then after 4 h $|J|$ gradually decreased to ~10 mA cm^{-2} (**Figure 4b and Figure S12b**). After CA, the *J-E* behavior of the illuminated p-GaAs/Pt_{ed}(0.5) electrode showed complete loss of photoactivity and J_{ph}, resembling the *J-E* behavior of a Pt electrode (**Figure 4a**). SEM imaging after CA revealed a smooth surface morphology with only a few particles (**Figure 4c**).

XPS analyses of the p-GaAs/Pt_{ed}(0.5) electrode after CA revealed substantial enrichment of As^0 (As^0/As=0.53±0.13) at the electrode surface, as well as relatively small Ga $2p_{3/2}$ and 3d signals (**Figure 4d-f and Figure S13**). The As 3d XPS data showed three doublets at BE = 41.3, 41.8, and 42.7 eV attributable to the As^{3-} anions of GaAs, As^0 and AsO_x, respectively (**Figure 4e**). A doublet at BE = 19.0 eV, assigned to Ga^{3+}, was observed in the Ga 3d XP spectrum, whereas a new doublet peak at BE = 17.0 eV was likely due to In impurities (**Figure 4f**). During the 4 h CA, the amounts of dissolved Ga and As ions in the electrolyte increased at rates corresponding to electrode dissolution of ~0.9 and ~0.2 nm h^{-1}, respectively (**Figure S14**).

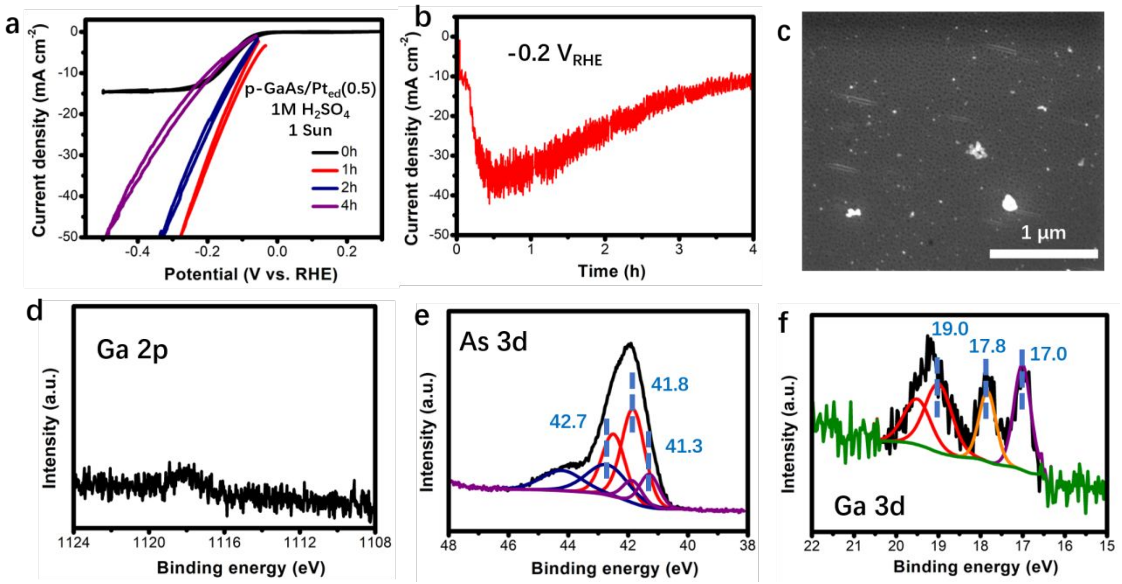

Figure 4. Results of a p-GaAs/Pt_{ed}(0.5) electrode evaluated in acidic electrolyte. (a) Changes in the *J-E* behavior over time and (b) CA of a p-GaAs/Pt_{ed}(0.5) electrode at -0.2 V vs. RHE in 1.0 M H_2SO_4(aq) under simulated 1-sun illumination. (c) SEM image of the p-GaAs/Pt_{ed}(0.5) electrode after CA. (d-f) XPS data in the (d) Ga $2p_{3/2}$, (e) As 3d, (f) Ga 3d regions for the illuminated p-GaAs/Pt_{ed}(0.5) electrode after CA in (b).

Figure 5a presents a cross-sectional transmission-electron microscopy (TEM) image of the p-GaAs/Pt_{ed}(0.5) electrode after the 4 h CA in 1.0 M H_2SO_4(aq). An amorphous region with a thickness of ~4 nm conformally covered the crystalline GaAs substrate, corresponding to the surface transformation revealed by the XPS data. The EDS line scan and mapping consistently revealed four different layers at the surface region of p-GaAs: GaAs/$Ga_{1-x}As$/GaO_x/As:Pt (**Figure 5b-c**). Moving from bulk GaAs towards the electrode surface, the Ga concentration gradually decreased and the As concentration increased, producing an As-rich layer ($Ga_{1-x}As$). The As concentration then decreased to almost zero, indicating a GaO_x layer with a Ga/O ratio of ~1.2, close to that of the Ga_2O_3 phase. Consistent with the XPS data, the outermost layer (As:Pt) consisted of a mixture of As and Pt (As/Pt ~3.1).

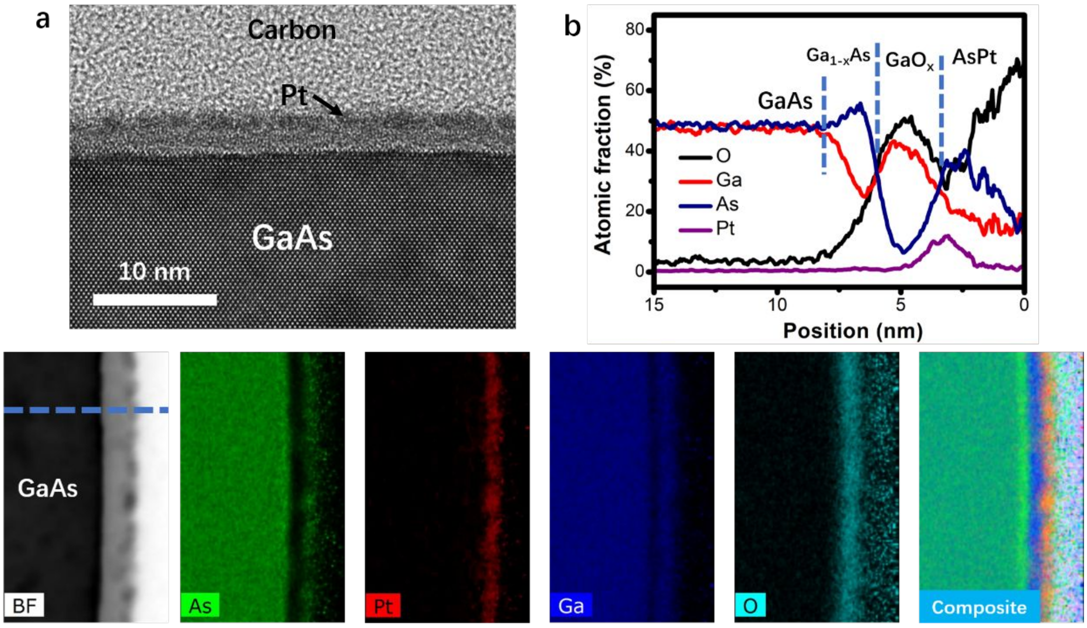

Figure 5. (a) cross-sectional TEM image, (b) EDS line scan and (c) EDS mapping across the surface of the p-GaAs/Pt_{ed}(0.5) electrode after the 4-h CA in 1.0 M H_2SO_4(aq).

In 1.0 M KOH(aq), the *J-E* behavior of a p-GaAs/Pt_{ed}(0.5) electrode was the same under illumination and in the dark, and in both cases showed no J_{ph}, indicating a loss of photoactivity (**Figure 6a**). For comparison, an etched p-GaAs electrode in the dark exhibited negligible J within the same E range in 1.0 M KOH(aq) (**Figure S8c**). During CA at -0.2 V vs. RHE, an illuminated p-GaAs/Pt$_{ed}$(0.5) electrode showed $J = -0.42 \pm 0.06$ mA cm^{-2} over 4 h (**Figure 6b**). The J-E behavior of the electrode remained constant during CA (**Figure 6c**). Slightly more As than Ga ions were detected in the electrolyte, with a dissolution rate of ~0.3 nm h^{-1} (**Figure S15a**). After CA, XPS data of the Ga 2p$_{3/2}$ and 3d regions showed additional peaks attributable to GaO$_x$, with signals at higher BE than those assigned to the Ga^{3+} cations of GaAs (**Figure 6d-f**). The XP spectrum in the As 3d region showed a substantial amount of As^0 (As^0/As=0.44±0.03) with observable AsO$_x$ (**Figure 6f**). The AFM image of p-GaAs/Pt$_{ed}$(0.5) electrode after CA showed distinct particles that were sparsely distributed over the electrode surface (**Figure S15b**).

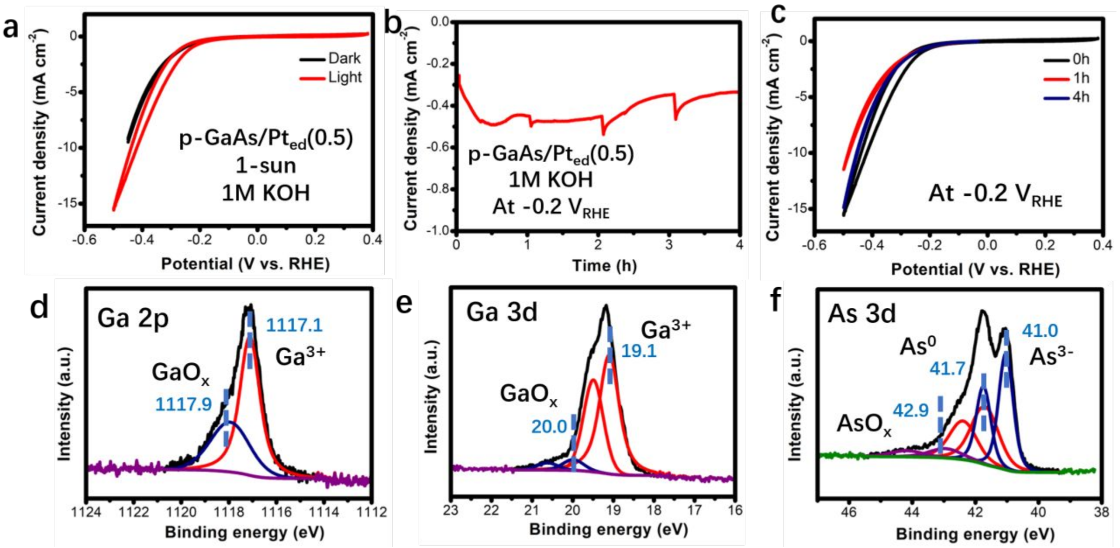

Figure 6. Results of a p-GaAs/Pt$_{ed}$(0.5) electrode evaluated in alkaline electrolyte. (a) Comparison of the J-E behavior for a p-GaAs/Pt$_{ed}$(0.5) electrode in 1.0 M KOH(aq) under simulated 1-sun illumination and in the dark. (b) CA of a p-GaAs/Pt$_{ed}$(0.5) electrode at -0.2 V vs. RHE in 1.0 M KOH(aq) under simulated 1-sun illumination, and (c) comparison of the J-E behavior measured periodically during CA in (b). (d-f) XPS data of the (d) Ga 2p$_{3/2}$, (e) Ga 3d and (f) As 3d regions for the p-GaAs/Pt$_{ed}$(0.5) electrode after CA in (b).

Stability of p-GaAs/Pt$_{ed}$(5) electrodes under simulated 1-sun illumination at -0.2 V vs. RHE.

A p-GaAs/Pt$_{ed}$(5) electrode was evaluated at E = -0.2 V vs. RHE in 1.0 M H_2SO_4(aq) under simulated 1-sun illumination (**Figure 7**). Prior to CA, the first three *J-E* cycles of an illuminated p-GaAs/Pt_{ed}(5) electrode showed rapid changes at $E \leq -0.2$ V vs. RHE (**Figure 7a**). Although the first *J-E* cycle showed $J_{ph} \sim -18$ mA cm^{-2}, the third *J-E* cycle appeared similar to the behavior of the p-GaAs/Pt_{ed}(0.5) electrode after CA in H_2SO_4. The anodic waves at $E > 0$ V vs. RHE are consistent with the oxidation of H_2 by Pt (**Figure 7a**). Initially the electrode exhibited $E_{oc} = 0.46$ V vs. RHE, but shortly after the CA, E_{oc} decreased to ~0 V vs. RHE. After the decrease in E_{oc}, the electrode exhibited the same *J-E* behavior in the dark as under illumination.

During CA, the *J-E* behavior of the p-GaAs/Pt $_{ed}$(5) electrode was periodically measured and remained similar to the third *J-E* cycle that had been measured before CA (**Figure 7c**). ICP-MS analysis revealed a higher amount (>2 nm) of dissolved Ga than As, and the As dissolution remained negligible (**Figure S16a**). After 50 h of CA, XPS data showed no peaks in the Ga 3d or 2p regions (**Figure 7d-e**), whereas the As 3d region showed a single doublet at BE = 42.1 eV representing As^0 (**Figure 7f**). After CA, the electrode surface appeared flat in the SEM image (**Figure S16b**), whereas the AFM image revealed a nanoparticulate morphology (**Figure S17**). After 48 h of CA in 1.0 M H_2SO_4(aq), a second p-GaAs/Pt_{ed}(5) electrode produced similar electrochemical behavior and surface characteristics to that of the first electrode (**Figure S18**).

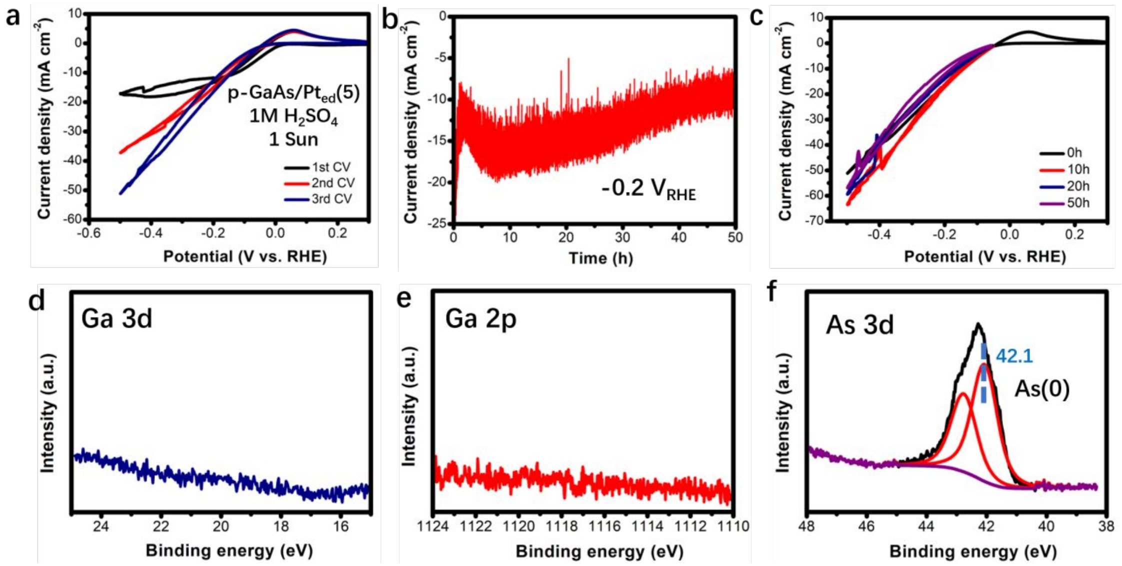

Figure 7. Results of a p-GaAs/Pt_{ed}(5) electrode evaluated in acidic electrolyte. (a) The first three *J-E* cycles of a p-GaAs/Pt_{ed}(5) electrode under simulated 1-sun illumination in 1.0 M H_2SO_4(aq) (scan rate: 50 mV s^{-1}). (b) CA of a p-GaAs/Pt_{ed}(5) electrode held at -0.2 V vs. RHE in 1.0 M H_2SO_4(aq) under simulated 1-sun illumination and (c) Comparison of its *J-E* behavior under simulated 1-sun illumination measured periodically during CA in (b) (scan rate: 50 mV s^{-1}). (d-f) XP spectra in the (d) Ga 3d, (e) Ga $2p_{3/2}$ and (f) As 3d regions

collected at the p-GaAs/Pt$_{ed}$(5) electrode surface after CA in (b).

In 1.0 M KOH(aq), the initial *J-E* cycles of an illuminated p-GaAs/Pt$_{ed}$(5) electrode displayed a similar shunting-type behavior to the p-GaAs/Pt$_{ed}$(0.5) electrode (**Figure 8a**). During CA at -0.2 V vs. RHE under illumination, the p-GaAs/Pt$_{ed}$(5) electrode showed J = -0.8±0.1 mA cm^{-2} (**Figure 8b**), and the *J-E* behavior remained unchanged over 24 h (**Figure 8c**). The apparent fluctuations in J are due to the periodic cyclic voltammetric measurements during the long-term CA experiments. Except for an initial dissolution of ~1 nm, ICP-MS analysis did not show evidence of continuous dissolution of Ga and As ions in the electrolyte **(Figure S19a)**. After CA, XPS data revealed an increase in the amount of As^0 (As^0/As=0.67±0.11) as well as newly formed GaO$_x$ (**Figure 8d-f**). The peak at BE = 531.5 eV in the O 1s XP spectrum corresponded to surficial GaO$_x$ **(Figure S20)**.[48,49] AFM images for the p-GaAs/Pt$_{ed}$(5) electrode showed a densely packed nanoparticulate morphology after CA **(Figure S19b)**. These results collectively demonstrate that further increases in the loading of electrodeposited Pt produced minimal impact on the electrochemical behavior of the resulting p-GaAs/Pt electrodes, and minimally impacted the changes in surface composition after long-term CA in either acidic and alkaline electrolytes.

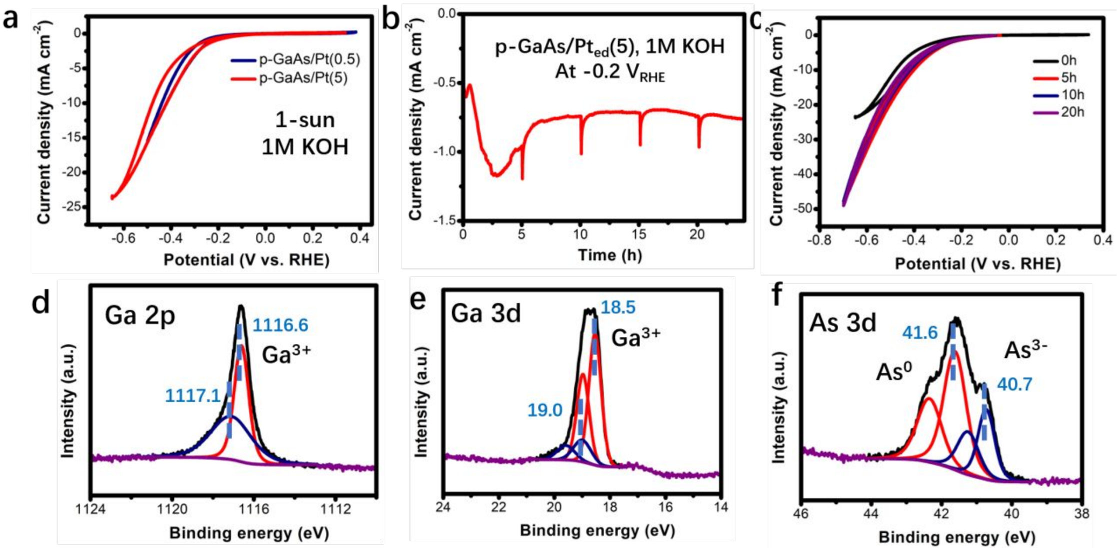

Figure 8. Results of a p-GaAs/Pt$_{ed}$(5) electrode evaluated in alkaline electrolyte. (a) Comparison of the *J-E* behavior before CA for a p-GaAs/Pt$_{ed}$(0.5) and a p-GaAs/Pt$_{ed}$(5) electrode in 1.0 M KOH(aq) under simulated 1-sun illumination. (b) CA of a p-GaAs/Pt$_{ed}$(5) electrode at -0.2 V vs. RHE in 1.0 M KOH(aq) under simulated 1-sun illumination and (c) comparison of CVs periodically measured during CA in (b). (d-f) XP spectra of the (d) Ga 2p$_{3/2}$, (e) Ga 3d and (f) As 3d regions for the p-GaAs/Pt$_{ed}$(5) electrode after CA in (b).

Stability of p-GaAs/Pt$_{sp}$(5) under simulated 1-sun illumination at -0.2 V vs. RHE.

p-GaAs electrodes with 5 nm of sputtered Pt, p-GaAs/Pt$_{sp}$(5), were evaluated under simulated 1-sun illumination at E = -0.2 V vs. RHE in 1.0 M H_2SO_4(aq) or 1.0 M KOH(aq). In both electrolytes, p-GaAs/Pt$_{sp}$(5) electrodes showed similar *J-E* behavior in the dark and under illumination, indicating a loss of photoactivity (**Figure S21**). Within the first 5 h of CA at -0.2 V vs. RHE, $|J|$ of p-GaAs/Pt$_{sp}$(5) electrodes decreased to <0.1 mA cm^{-2} in both electrolytes (**Figure S22a-b**). In 1.0 M H_2SO_4(aq), the *J-E* behavior of p-GaAs/Pt$_{sp}$(5) electrodes displayed pronounced changes during CA (**Figure 9a**), whereas in 1.0 M KOH(aq), the *J-E* behavior remained nearly unchanged throughout the CA (**Figure 9b**).

XPS data of an as-prepared p-GaAs/Pt$_{sp}$(5) sample exhibited two As 3d doublets at BE = 40.6 eV (GaAs) and BE = 41.4 eV (As^0), with a Ga/As ratio of 1.24 and an As^0/As ratio of 0.58±0.3. After CA, surface enrichment of As with predominantly As^0 was observed for electrodes in either acidic (Ga/As=0.11) or alkaline (Ga/As =0.38) electrolytes (**Figure 9c-e**). Notably, after the CA in 1.0 M KOH(aq), a substantial amount of AsO$_x$ (BE = 43.8 eV) appeared on the p-GaAs/Pt$_{sp}$(5) electrode. For both samples, dissolution of GaAs plateaued at ~10 nm after 10 h (**Figure S22c-d**). SEM images of the p-GaAs/Pt$_{sp}$(5) electrodes revealed minimal changes in surface morphology after CA in acid, but in 1.0 M KOH(aq) dissolution pits were observed after the CA (**Figure S23**).

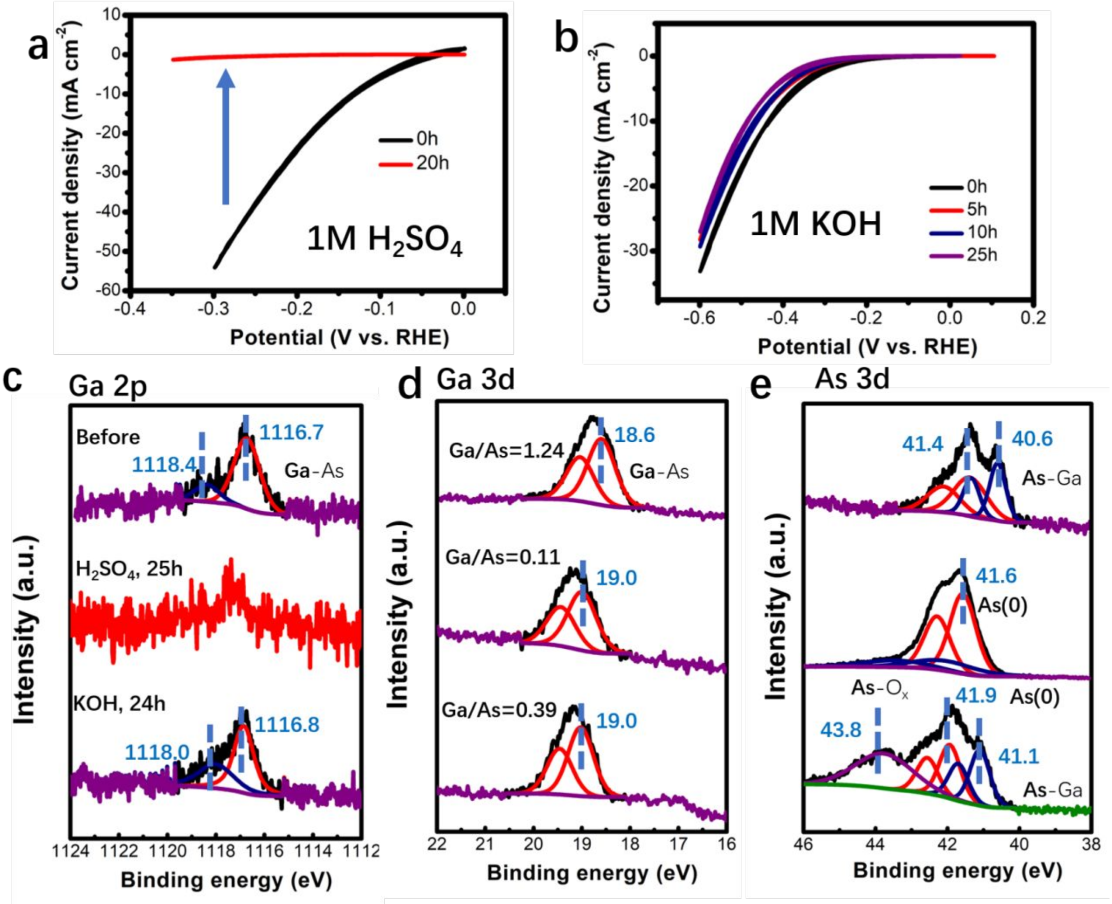

Figure 9. Results of p-GaAs/Pt$_{sp}$(5) electrodes evaluated in acidic and alkaline electrolytes. (a-b) Comparison of the *J-E* behavior over time of illuminated p-GaAs/Pt$_{sp}$(5) electrodes (1 sun) during CA at E=-0.2 V vs. RHE in (a) 1.0 M H_2SO_4(aq) and (b) 1.0 M KOH(aq). (c-e) XP spectra in the (c) Ga 2p$_{3/2}$, (d) Ga 3d and (e) As 3d regions for p-GaAs/Pt$_{sp}$(5) electrodes before and after CA in (a-b).

Preparation and characterization of p-GaAs/CoP electrodes.

To compare to the behavior of platinized GaAs electrodes, another HER catalyst, CoP, was photoelectrodeposited onto the surface of p-GaAs.[38] Three different p-GaAs/CoP(*x*) electrodes were prepared, with *x* representing the charge density passed during deposition (x = 50, 200 or 400 mC cm^{-2}). The CA of CoP deposition for the three electrodes is shown in **Figure S24a**. At E < -0.1 V vs. RHE, the dark cathodic *J* of p-GaAs/CoP electrodes in 1.0 M H_2SO_4(aq) increased substantially as the loading of CoP increased from 50 to 400 mC cm^{-2} (**Figure S24b**). SEM imaging of an as-prepared p-GaAs/CoP(200) electrode showed a thin-film morphology with cracks (**Figure S25a**). The CoP thin-film was composed of individual islands, with each island formed by an aggregate of small nanoparticles (**Figure S25b**).

For an as-prepared p-GaAs/CoP(200) electrode, XPS data in the Ga $2p_{3/2}$ and 3d regions showed peaks at BE = 1116.9 and 18.7 eV, respectively, ascribable to the Ga^{3+} cations of GaAs (**Figure S28**). The As 3d region exhibited peaks for the As^{3-} anions of GaAs and As^0 at BE = 40.5 and 41.0 eV, respectively. The Ga/As ratio was 0.7, whereas the As^0/As was 0.22±0.15. The low signal-to-noise ratios in the Ga and As XP spectra were due to the thick coating of CoP. In the Co 2p region, the peaks at BE = 777.8 and 780.4 eV are assigned to metallic Co^0 and CoO_x, respectively.[38] The P 2p region showed peaks at BE = 129.1 and 129.9 eV attributable to CoP, and showed peaks at BE = 131.5 and 133.0 eV indicative of a Co orthophosphate compound.

Stability of p-GaAs/CoP electrodes under simulated 1-sun illumination at -0.2 V vs. RHE in acid.

A comparison of the *J-E* behavior of three p-GaAs/CoP electrodes revealed decreases in photocurrent density as well as increases in dark cathodic *J* as the loading of CoP increased on the electrode surface (**Figure 10a-c**). During CA at -0.2 V vs. RHE, all three p-GaAs/CoP(*x*) electrodes exhibited stable *J* under simulated 1-sun illumination **(Figure 10d-f)**, and their *J-E* behavior was essentially constant during CA (**Figure 10g-i**). After CA, the p-GaAs/CoP(400) electrode displayed a similar morphology to the as-prepared p-GaAs/CoP(200) electrode, whereas the surface of both p-GaAs/CoP(50) and p-GaAs/CoP(200) electrodes showed sparsely distributed particles (**Figure S26-27**).

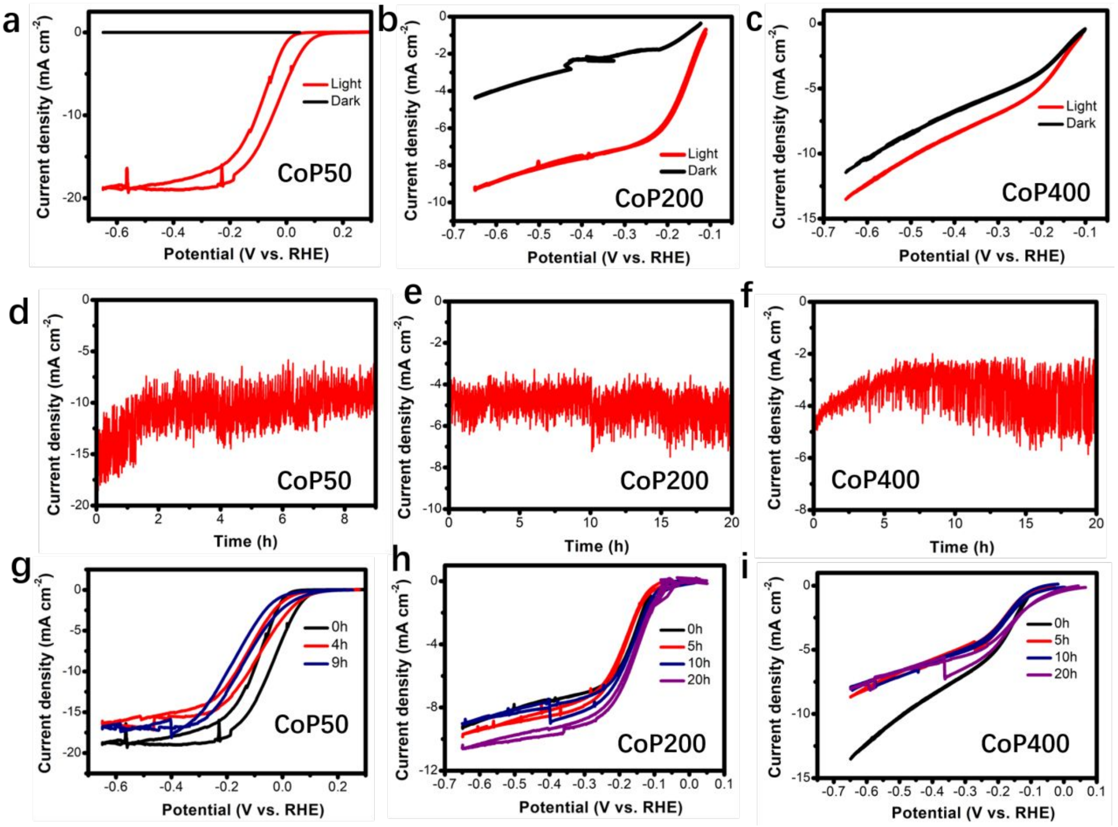

Figure 10. Results of p-GaAs/CoP electrodes evaluated in acidic electrolytes. (a-c) Comparison of the *J-E* behavior of (a) a p-GaAs/CoP(50), (b) a p-GaAs/CoP(200) and (c) a p-GaAs/CoP(400) electrode, measured in the dark and under simulated 1-sun illumination in 1.0 M H_2SO_4(aq) (d-f) CA of (a) a p-GaAs/CoP(50), (b) a p-GaAs/CoP(200) and (c) a p-GaAs/CoP(400) electrode at -0.2 V vs. RHE under simulated 1-sun illumination in 1.0 M H_2SO_4(aq). (g-i) Comparison of the *J-E* behavior periodically measured during the CA of (a) p-GaAs/CoP(50), (b) p-GaAs/CoP(200) and (c) p-GaAs/CoP(400) electrodes.

Figure 11 shows XPS analyses of the three p-GaAs/CoP electrodes after CA. For the p-GaAs/CoP(200) electrode, the increased signal-to-noise ratios in the Ga and As XP spectra after CA indicated partial dissolution of the CoP deposit during the HER in the acidic electrolyte, consistent with the observed decrease in the Co/As atomic ratio from 39.7 to 0.6.[50] The Co^0 peak at BE = 777.8 eV disappeared in the Co 2p XP spectrum, whereas a new peak emerged at BE = 778.8 eV, ascribable to CoP.[38] After CA the PO_x peak at BE = 133.0 eV in the P 2p XP spectrum became more pronounced relative to the CoP peaks at BE = 129.1 and 129.9 eV. Moreover, a GaO_x signal appeared in the Ga $2p_{3/2}$ region at BE = 1118.5 eV (**Figure S28**).

After CA, the XP spectra of the p-GaAs/CoP(50) and p-GaAs/CoP(400) electrodes were similar to those of the p-GaAs/CoP(200) electrode. In contrast to the p-GaAs/Pt electrodes, the As 3d XP spectra for p-GaAs/CoP(*x*) electrodes showed no increase in surficial As^0. Consistently, both the p-GaAs/CoP(50) (Ga/As = 1.03) and p-GaAs/CoP(200) (Ga/As = 0.89) electrodes displayed nearly stochiometric GaAs surfaces. After operation of the HER, the deposited CoP, along with PO_x (BE > 132 eV), remained at the surface of p-GaAs/CoP(*x*)electrodes. After CA on the p-GaAs/CoP(400) electrode, the Ga and As XPS data showed much weaker signals due to the CoP coating, with substantial AsO_x (BE=43.3 eV) signals in the As 3d region.

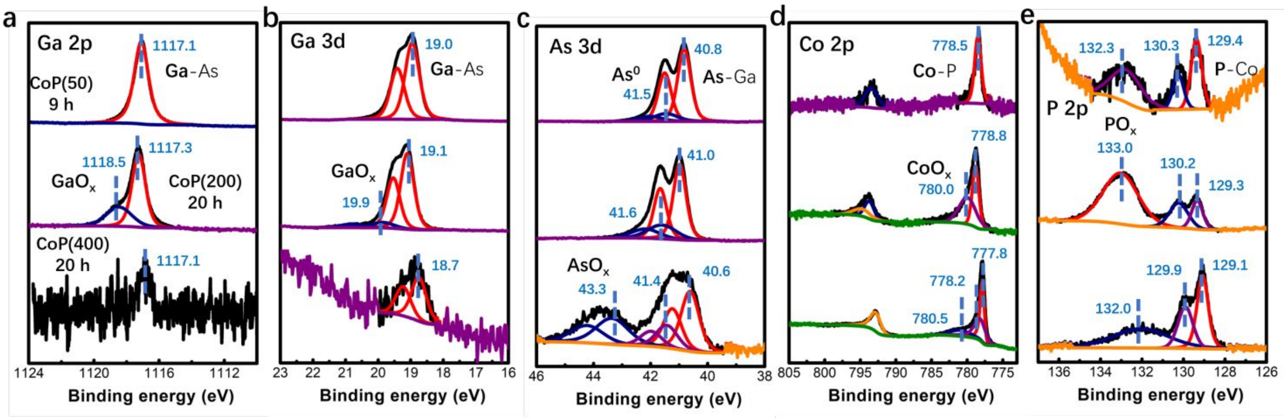

Figure 11. Comparison of XP spectra in the (a) Ga $2p_{3/2}$, (b) Ga 3d, (c) As 3d, (d) Co 2p and (e) P 2p regions for three different p-GaAs/CoP electrodes after CA at -0.2 V vs. RHE in 1.0 M H_2SO_4(aq) under simulated 1-sun illumination: p-GaAs/CoP(50) after 9 h (upper panels), p-GaAs/CoP(200) after 20 h (middle panels) and p-GaAs/CoP(400) after 20 h (bottom panels).

Discussion

GaAs dissolution under E_{oc} and negative E: The thermodynamic Pourbaix diagram (**Figure S1**) is useful for determining corrosion pathways of GaAs at a given pH and *E*.[51] Herein, we focus on the stability of GaAs under conditions of the HER ($E < 0$ V vs. RHE) at pH = 0 and pH = 14. A calculated Pourbaix diagram for GaAs by the Materials Project predicts a stable GaAs phase at $E <$ -0.4 V vs. RHE across the whole pH range (**Figure S1)**, indicating cathodic protection. However, $E \geq$ -0.1 V vs. RHE favors the oxidation of GaAs to soluble As(III) and Ga(III) ions (Eq 2a-b), whereas $-0.4 < E < -0.1$ V vs. RHE results in formation of elemental As^0 and Ga(III) ions (Eq 3a-b).

pH = 0, E >-0.1 V_{RHE}: $2GaAs(s) + 4H_2O(l) + 6H^+(aq) \rightarrow 2Ga^{3+}(aq) + 2HAsO_2(aq) + 6H_2(g)$

(2a)

pH = 14, E >-0.2 V_{RHE}: $GaAs(s) + 4OH^-(aq) + 2H_2O(l) \rightarrow GaO_3^{3-}(aq) + H_2AsO_3^-(aq) + 3H_2(g)$

(2b)

pH = 0, -0.5<E<-0.1 V_{RHE}: $2GaAs(s) + 6H^+(aq) \rightarrow 2Ga^{3+}(aq) + 2As^0(s) + 3H_2(g)$

(3a)

pH = 14, -0.4<E<-0.2 V_{RHE}: $2GaAs(s) + 6OH^-(aq) \rightarrow 2GaO_3^{3-}(aq) + 2As^0(s) + 3H_2(g)$

(3b)

The results of electrode dissolution and XPS surface analyses are summarized in **Table S1** and **S2**, respectively. In the dark, etched n- and p-GaAs electrodes showed positive values of E_{oc} (+0.1 to +0.5 V vs. RHE), as well as continuous and stoichiometric dissolution at rates of <1 and ~6 nm h^{-1} in acidic and alkaline electrolytes, respectively. Based on the measured E_{oc} values, the corrosion reactions of GaAs should follow Eq 2a-b, with the oxidation of GaAs by water or protons forming soluble Ga and As ions at both pH = 0 and pH = 14.

Compared with the conditions of E_{oc}, the CA experiments of n-GaAs electrodes at E = -0.1 V vs. RHE in the dark showed negligible dissolution over long periods in either acidic or alkaline electrolytes. The Pourbaix diagram in **Figure S1** predicts that the formation of As^0 is likely at E = -0.1 V vs. RHE for both pH = 0 and pH=14, following **Eq 3a-b**. However, only a small increase of As^0 was observed at the surface of the n-GaAs electrode evaluated in 1.0 M H_2SO_4(aq). These results suggest that applying a potential of E = -0.1 V vs. RHE to n-GaAs electrodes mitigates the continuous dissolution at E_{oc} in the dark, whereas the kinetics of As^0 formation is slow for etched n-GaAs electrodes.

Maintaining illuminated etched p-GaAs electrodes at negative potentials (E = -0.2 or -0.6 V vs. RHE) also resulted in little continuous corrosion of GaAs (**Table S1**). Notably, the p-GaAs electrodes maintained photoactivity after operation of the HER, with minimal surface changes and without detectable formation of excess As^0 (**Scheme 1a**). Considering the slow kinetics of the HER at the surface of etched GaAs, these results indicate that the surface potential of p-GaAs photoelectrodes during the HER is more negative than the E region that favors As^0 formation, thereby enabling cathodic protection of GaAs. For etched p-GaAs photoelectrodes in acidic electrolytes, slow rates of dissolution (~0.1 nm h^{-1}) were observed only for Ga ions. Previous spectroscopic studies have revealed that at etched GaAs surfaces the HER occurs via As-H interactions.[52,53] Thus, the absence of As ions in the electrolyte can consistently be attributed to the $AsH_3(g)$ formation under negative E (Eq 4), whereas the AsH_3 is carried away by the concurrent $H_2(g)$ evolution from electrode surface.[54]

$$\text{pH=0:}\ \ \mathrm{GaAs(s)} + 3\mathrm{H^+(aq)} \rightarrow \mathrm{AsH_3} + \mathrm{Ga^{3+}(aq)} \qquad (4)$$

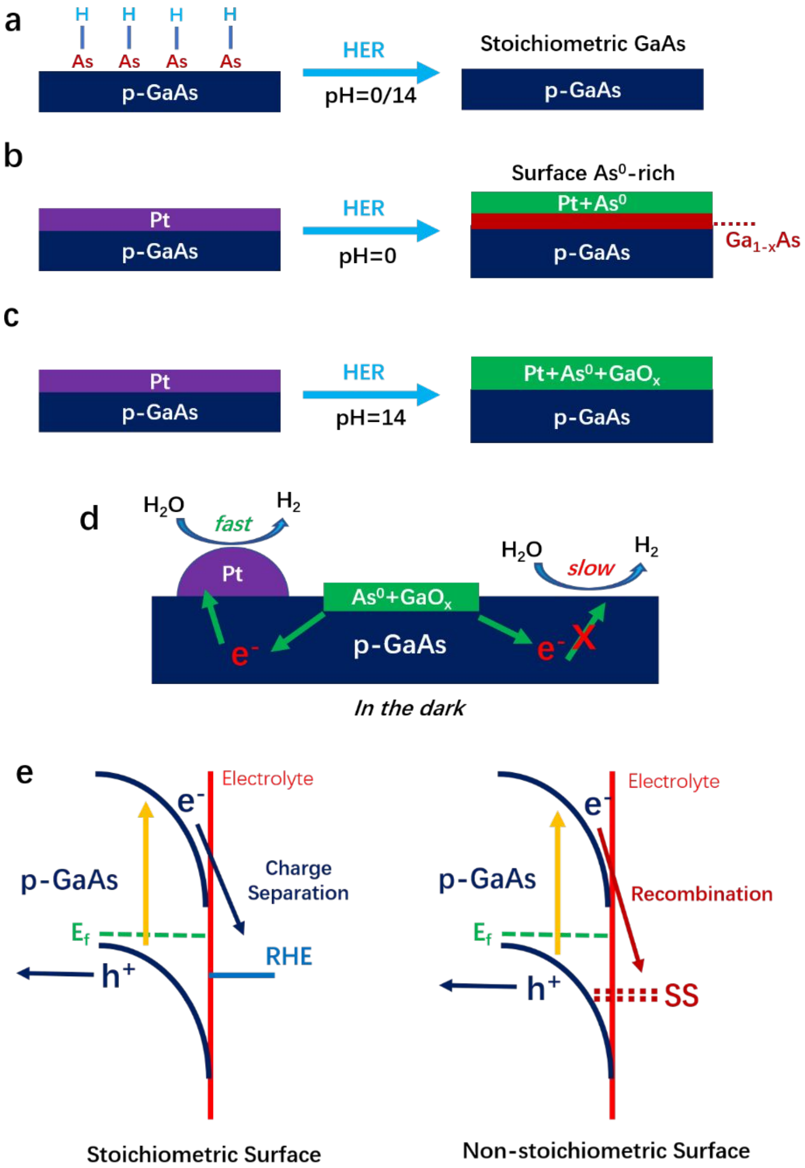

Scheme 1. (a-c) Schematic illustration of the changes of surface conditions for (a) etched p-GaAs and (b-c) p-GaAs/Pt electrodes before and after operation of the HER under illumination at pH=0 and pH=14. (d) Galvanic corrosion of GaAs forming surficial As^0 and GaO_x species assisted by Pt catalyst. (e) Comparison of band energy diagram of illuminated p-GaAs electrodes with a stoichiometric or a non-stoichiometric surface under cathodic bias; a stoichiometric GaAs surface promotes effective charge separation, whereas charge

recombination occurs for a non-stoichiometric GaAs surface due to surface states (SS).

Pt-induced As^0 formation causes a loss in the p-GaAs photoactivity: As shown by the XPS data, electrodeposition of Pt at a p-GaAs surface leads to the formation of excess As^0 under conditions of the HER at both pH = 0 and pH = 14. p-GaAs/Pt_{ed}(0.5) and p-GaAs/Pt_{ed}(5) electrodes yielded mutually similar electrochemical behavior and surface characteristics after CA in 1.0 M H_2SO_4(aq) or 1.0 M KOH(aq). These results indicate that a small amount of Pt (0.5 nm) facilitates the surface conversion of GaAs into As^0. After CA at pH=0, As^0 was primarily observed for p-GaAs/Pt_{ed} electrodes (**Scheme 1b**), whereas after CA at pH=14 both GaO_x and As^0 formed at the surface of p-GaAs/Pt_{ed} electrodes (**Scheme 1c**). Hence, at pH=14 the Ga(III) species in Eq 3d manifested as insoluble oxides (GaO_x) instead of as GaO_3^{3-} ions. The absence of GaO_x on the electrode surface at pH = 0 is consistent with the high solubility of oxidized Ga under these conditions, resulting in a larger amount of Ga than As ions detected by ICP-MS in the electrolyte.

Sputtering of Pt at room temperature onto the surface of etched p-GaAs directly induced the formation of excess As^0 prior to electrochemical measurements, causing electrode shunting with no photoactivity. This behavior indicates the presence of a solid-state reaction between Pt and GaAs during the deposition process. After CA, the surfaces of p-GaAs/Pt_{sp} electrodes became even more As-rich, as shown by the decreased Ga/As ratios at either pH = 0 or pH = 14.

For all p-GaAs/Pt electrodes, the formation of excess surficial As^0 concurrently led to (1) loss of photoactivity, (2) emergence of dark cathodic J for the HER, and (3) shunting behavior in either acidic or alkaline electrolytes. For comparison, over the same E range, etched p-GaAs electrodes initially displayed negligible J in the dark, as well as a well-defined J_{ph} of ~-20 mA cm^{-2} under illumination. Collectively, these results demonstrated the importance of the surface chemistry of GaAs towards defining the electrical characteristics of the resulting electrodes.

Based on the unified defect model proposed by Spicer and coworkers,[55] the electronic properties of GaAs are sensitive to changes in surface stoichiometry. Excess As or Ga atoms at GaAs surfaces produce mid-gap surface states (SS), located at 0.5 eV and 0.75 eV above the valence band maximum (VBM), respectively.[56] The experimental observations herein are consistent with this model, as the *J-E* behavior of p-GaAs electrodes is highly dependent on changes in the electrode surface under conditions of the HER. The conduction-band edge of GaAs has been estimated to be 0.8 to 1.0 eV more negative than the potential of RHE, whereas the relative positions of the conduction-band edge and the RHE potentials are fixed as the pH is varied.[57–60] The low PEC performance of p-GaAs photocathodes is thus consistent with a low barrier height between the Fermi level potential (E_f) of p-GaAs and the RHE potential in the various aqueous electrolytes. As shown in **Scheme 1e**, etched p-GaAs electrodes maintain nearly stoichiometric surfaces as well as photoactivity under cathodic current flow, resulting in effective separation of photogenerated electrons.[61,62] For p-GaAs/Pt electrodes, the formation of either surficial As^0 (shown by XPS), or an As-rich interlayer (shown by TEM) during the HER, results in surface states at a non-stoichiometric GaAs surface. The mid-gap surface states create a recombination pathway for photogenerated electrons, thereby leading to a loss in photocurrent (**Scheme 1e**). Moreover, such surface states also provide a shunting pathway for passing dark cathodic *J* through the Pt catalyst at negative *E*, due to the similar energy levels of the surface states to the potential of the RHE. Additionally, the increased *J* measured in the dark for etched p-GaAs photocathodes after the HER operation for >4 h in 1.0 M KOH(aq) is also likely attributable to the slight Ga-enrichment at the electrode surface.

Collectively, these results indicate that the Pt catalyst facilitates the oxidation of GaAs to As^0 via **Eq.** 3a-b by an interfacial galvanic pathway (**Scheme 1d**).[23] This pathway results from the facile HER kinetics of Pt, which also lowers the surface potential of p-GaAs into the thermodynamic *E* region that favors formation of As^0. In contrast, the slow HER kinetics at an etched GaAs surface inhibits such a corrosion pathway, as supported by the results for n-GaAs electrodes in the dark at *E* = -0.1 V vs. RHE. Consequently, both thermodynamic and kinetic factors of the Pt catalyst promote the formation of As^0.

Despite the surface transformations, sustained dissolution of GaAs remained slow for etched p-GaAs electrodes as well as for Pt-coated electrodes passing cathodic current in acidic or alkaline electrolytes. p-GaAs (photo)-cathodes are thus physically robust when performing the HER at negative *E* at pH = 0 or at pH = 14. In contrast, GaAs rapidly corrodes anodically or continuously dissolves at E_{oc} in the dark (**Table S1**).[21] Furthermore, although analogous to metal-assisted chemical etching (MacEtch), the corrosion of GaAs to As^0 induced by Pt is self-limiting and does not involve continuous dissolution, while requiring no oxidant other than H_2O or H^+.[63–65]

Comparison of CoP and Pt catalysts: Excess As^0 was not observed for p-GaAs/CoP electrodes after operation of the HER in acidic electrolytes. This behavior indicates that the p-GaAs/CoP/H_2O tri-phase interface does not result in the same galvanic corrosion pathway as occurs for p-GaAs/Pt/H_2O tri-phase interfaces. Despite the slightly lower HER activity of CoP than Pt, the overpotentials at J = -10 mA cm^{-2} of both catalysts should be within or near the E range that favors formation of As^0.[38] Compared to metallic Pt, the lack of As^0 formation for CoP is consistent with the low conductivity of CoP and/or a different coverage configuration on GaAs (thin-film vs. nano-particulate), resulting in a lack of ability to form local redox centers that are in good electrical communication with the substrate. Use of the earth-abundant CoP catalyst instead of the noble-metal Pt catalyst on p-GaAs also provides a constructive example situation in which an unfavorable surface conversion of GaAs can be mitigated by tailoring the morphology and composition of the HER catalyst. However, the increases in dark J of p-GaAs/CoP electrodes as the CoP loading is increased indicates an unfavorable band alignment at the interface, which will require further interface engineering techniques to optimize both the stability and high performance of such systems as photocathodes for solar fuels production.

Conclusions

The long-term stability of p-GaAs photocathodes for the HER has been evaluated in contact with acidic and alkaline electrolytes, with or without active catalysts (Pt or CoP). After operation of the HER at either pH = 0 or pH = 14, illuminated etched p-GaAs electrodes maintained nearly stoichiometric surfaces as well as photoactivity. However, electrodeposition or sputtering of Pt onto p-GaAs surfaces led to the formation of excess As^0 via an interfacial galvanic reaction. p-GaAs/Pt electrodes with surficial As^0 displayed a shunting type behavior as well as a deleterious loss of photoactivity. In contrast, p-GaAs electrodes coated with a thin-film of CoP catalyst did not produce excess As^0 after performing the HER in acidic electrolytes. Under cathodic current flow, illuminated p-GaAs electrodes exhibited negligible dissolution during long-term operation at pH = 0 or pH = 14, however the *J-E* behavior degraded due to the changes in surface stoichiometry. This work reveals the importance of surface characteristics for determining the photoelectrochemical behavior of p-GaAs electrodes, and underscores the importance of controlling and optimizing the electrocatalyst with the semiconductor to mitigate unfavorable interfacial reactions that affect the performance of otherwise stable photocathodes.

Acknowledgements

This material is based upon work performed by the Joint Center for Artificial Photosynthesis, a DOE Energy Innovation Hub, supported through the Office of Science of the U.S. Department of Energy under Award Number DE-SC0004993 and by award DE-SC0022087 from the DOE Office of Basic Energy Sciences. Research was in part performed in the Molecular Materials Resource Center (MMRC) of the Beckman Institute of the California Institute of Technology. Phil Jahelka and Dr. Chengxiang Xiang are gratefully acknowledged for fruitful discussions. Dr. Nathan Dalleska provided assistance with ICP-MS analysis and Dr. Pakpoom Buabthong assisted with XPS analysis.

References

1 J. R. McKone, N. S. Lewis and H. B. Gray, *Chemistry of Materials*, 2014, **26**, 407–414.

2 N. S. Lewis, *Nature Nanotechnology*, 2016, **11**, 1010.

3 M. G. Walter, E. L. Warren, J. R. McKone, S. W. Boettcher, Q. Mi, E. A. Santori and N. S. Lewis, *Chemical Reviews*, 2010, **110**, 6446–6473.

4 J. Jin, K. Walczak, M. R. Singh, C. Karp, N. S. Lewis and C. Xiang, *Energy Environ. Sci.*, 2014, **7**, 3371–3380.

5 D. Bae, B. Seger, P. C. Vesborg, O. Hansen and I. Chorkendorff, *Chem Soc Rev*, 2017, **46**, 1933–1954.

6 S. Hu, N. S. Lewis, J. W. Ager, J. Yang, J. R. McKone and N. C. Strandwitz, *The Journal of Physical Chemistry C*, 2015, **119**, 24201–24228.

7 M. F. Lichterman, K. Sun, S. Hu, X. Zhou, M. T. McDowell, M. R. Shaner, M. H. Richter, E. J.

Crumlin, A. I. Carim, F. H. Saadi, B. S. Brunschwig and N. S. Lewis, *Catalysis Today*, 2016, **262**, 11–23.

8 X. Zhou, R. Liu, K. Sun, D. Friedrich, M. T. McDowell, F. Yang, S. T. Omelchenko, F. H. Saadi, A. C. Nielander, S. Yalamanchili, K. M. Papadantonakis, B. S. Brunschwig and N. S. Lewis, *Energy & Environmental Science*, 2015, **8**, 2644–2649.

9 K. Sun, F. H. Saadi, M. F. Lichterman, W. G. Hale, H.-P. Wang, X. Zhou, N. T. Plymale, S. T. Omelchenko, J.-H. He, K. M. Papadantonakis, B. S. Brunschwig and N. S. Lewis, *Proceedings of the National Academy of Sciences*, 2015, **112**, 3612.

10 K. Sun, M. T. McDowell, A. C. Nielander, S. Hu, M. R. Shaner, F. Yang, B. S. Brunschwig and N. S. Lewis, *The Journal of Physical Chemistry Letters*, 2015, **6**, 592–598.

11 K. Sun, I. A. Moreno-Hernandez, W. C. Schmidt, X. Zhou, J. C. Crompton, R. Liu, F. H. Saadi, Y. Chen, K. M. Papadantonakis and N. S. Lewis, *Energy & Environmental Science*, 2017, **10**, 987–1002.

12 H. Gerischer, *Journal of Vacuum Science and Technology*, 1978, **15**, 1422–1428.

13 S. Hu, C. Xiang, S. Haussener, A. D. Berger and N. S. Lewis, *Energy & Environmental Science*, 2013, **6**, 2984–2993.

14 E. Verlage, S. Hu, R. Liu, R. J. R. Jones, K. Sun, C. Xiang, N. S. Lewis and H. A. Atwater, *Energy & Environmental Science*, 2015, **8**, 3166–3172.

15 S. Hu, M. R. Shaner, J. A. Beardslee, M. Lichterman, B. S. Brunschwig and N. S. Lewis, *Science*, 2014, **344**, 1005.

16 M. V. Lebedev, W. Calvet, T. Mayer and W. Jaegermann, *The Journal of Physical Chemistry C*, 2014, **118**, 12774–12781.

17 Y. Huang, J. Luo and D. G. Ivey, *Thin Solid Films*, 2006, **496**, 724–734.

18 Y. Huang, J. Luo and D. G. Ivey, *Materials Chemistry and Physics*, 2005, **93**, 429–442.

19 S. Y. Alqaradawi, A. S. Aljaber and M. M. Khader, *Thin Solid Films*, 2003, **444**, 282–289.

20 A. Kraft and K.-H. Heckner, *Journal of Radioanalytical and Nuclear Chemistry Articles*, 1994, **182**, 257–265.

21 P. Buabthong, Z. P. Ifkovits, P. A. Kempler, Y. Chen, P. D. Nunez, B. S. Brunschwig, K. M. Papadantonakis and N. S. Lewis, *Energy & Environmental Science*, , DOI:10.1039/D0EE02032J.

22 J. Zhang, J. Lai, W. Wang, P. Huang, J. Jia, L. Han, Z.-W. Tian, Z.-Q. Tian and D. Zhan, *The Journal of Physical Chemistry C*, 2017, **121**, 9944–9952.

23 J. Zhang, L. Zhang, W. Wang, L. Han, J.-C. Jia, Z.-W. Tian, Z.-Q. Tian and D. Zhan, *Chemical Science*, 2017, **8**, 2407–2412.

24 J. Lai, D. Yuan, P. Huang, J. Zhang, J.-J. Su, Z.-W. Tian and D. Zhan, *The Journal of Physical Chemistry C*, 2016, **120**, 16446–16452.

25 J. Zhang, L. Zhang, L. Han, Z.-W. Tian, Z.-Q. Tian and D. Zhan, *Nanoscale*, 2017, **9**, 7476–7482.

26 K. C. Chang, A. Heller, B. Schwartz, S. Menezes and B. Miller, *Science*, 1977, **196**, 1097–1099.

27 B. J. Tufts, I. L. Abrahams, P. G. Santangelo, G. N. Ryba, L. G. Casagrande and N. S. Lewis, *Nature*, 1987, **326**, 861–863.

28 S. Hu, C.-Y. Chi, K. T. Fountaine, M. Yao, H. A. Atwater, P. D. Dapkus, N. S. Lewis and C. Zhou, *Energy & Environmental Science*, 2013, **6**, 1879.

29 F. Yang, A. C. Nielander, R. L. Grimm and N. S. Lewis, *The Journal of Physical Chemistry C*, 2016, **120**, 6989–6995.

30 C. M. Gronet and N. S. Lewis, *Appl. Phys. Lett.*, 1983, **43**, 115–117.

31 B. J. Tufts, I. L. Abrahams, L. G. Casagrande and N. S. Lewis, *J. Phys. Chem.*, 1989, **93**, 3260–3269.

32 M. X. Tan, C. Newcomb, A. Kumar, S. R. Lunt, M. J. Sailor, B. J. Tufts and N. S. Lewis, *J. Phys. Chem.*, 1991, **95**, 10133–10142.

33 W.-H. Cheng, M. H. Richter, M. M. May, J. Ohlmann, D. Lackner, F. Dimroth, T. Hannappel, H. A. Atwater and H.-J. Lewerenz, *ACS Energy Letters*, 2018, **3**, 1795–1800.

34 F. R. F. Fan and A. J. Bard, *Journal of the American Chemical Society*, 1980, **102**, 3677–3683.

35 A. J. Bard, A. B. Bocarsly, F. R. F. Fan, E. G. Walton and M. S. Wrighton, *J. Am. Chem. Soc.*, 1980, **102**, 3671–3677.

36 J. L. Young, K. X. Steirer, M. J. Dzara, J. A. Turner and T. G. Deutsch, *Journal of Materials Chemistry A*, 2016, **4**, 2831–2836.

37 M. Ben-Naim, R. J. Britto, C. W. Aldridge, R. Mow, M. A. Steiner, A. C. Nielander, L. A. King, D. J. Friedman, T. G. Deutsch, J. L. Young and T. F. Jaramillo, *ACS Energy Letters*, 2020, **5**, 2631–2640.

38 F. H. Saadi, A. I. Carim, E. Verlage, J. C. Hemminger, N. S. Lewis and M. P. Soriaga, *The Journal of Physical Chemistry C*, 2014, **118**, 29294–29300.

39 M. C. Traub, J. S. Biteen, D. J. Michalak, L. J. Webb, B. S. Brunschwig and N. S. Lewis, *The Journal of Physical Chemistry B*, 2006, **110**, 15641–15644.

40 S. R. Lunt, G. N. Ryba, P. G. Santangelo and N. S. Lewis, *Journal of Applied Physics*, 1991, **70**, 7449–7467.

41 M. C. Traub, J. S. Biteen, D. J. Michalak, L. J. Webb, B. S. Brunschwig and N. S. Lewis, *The Journal of Physical Chemistry C*, 2008, **112**, 18467–18473.

42 P. A. Kempler, Z. P. Ifkovits, W. Yu, A. I. Carim and N. S. Lewis, *Energy Environ. Sci.*, 2021, **14**, 414–423.

43 P. A. Kempler, R. H. Coridan and N. S. Lewis, *Energy Environ. Sci.*, 2020, **13**, 1808–1817.

44 K. Choi, K. Kim, I. K. Moon, I. Oh and J. Oh, *ACS Applied Energy Materials*, 2019, **2**, 770–776.

45 Y. H. Lee, J. Kim and J. Oh, *ACS Applied Materials & Interfaces*, 2018, **10**, 33230–33237.

46 K. Choi, K. Kim, I. K. Moon, J. Bang and J. Oh, *Nanoscale*, 2019, **11**, 15367–15373.

47 K. C. Kwon, S. Choi, K. Hong, C. W. Moon, Y.-S. Shim, D. H. Kim, T. Kim, W. Sohn, J.-M. Jeon, C.-H. Lee, K. T. Nam, S. Han, S. Y. Kim and H. W. Jang, *Energy & Environmental Science*, 2016, **9**, 2240–2248.

48 S.-L. Ou, D.-S. Wuu, Y.-C. Fu, S.-P. Liu, R.-H. Horng, L. Liu and Z.-C. Feng, *Materials Chemistry and Physics*, 2012, **133**, 700–705.

49 D. Y. Guo, Z. P. Wu, Y. H. An, P. G. Li, P. C. Wang, X. L. Chu, X. C. Guo, Y. S. Zhi, M. Lei, L. H. Li and W. H. Tang, *Appl. Phys. Lett.*, 2015, **106**, 042105.

50 P. A. Kempler, H. J. Fu, Z. P. Ifkovits, K. M. Papadantonakis and N. S. Lewis, *The Journal of Physical Chemistry Letters*, 2020, **11**, 14–20.

51 K. A. Persson, B. Waldwick, P. Lazic and G. Ceder, *Physical Review B*, , DOI:10.1103/PhysRevB.85.235438.

52 B. H. Erné, F. Ozanam and J.-N. Chazalviel, *The Journal of Physical Chemistry B*, 1999, **103**, 2948–2962.

53 B. H. Erné, F. Ozanam and J.-N. Chazalviel, *Physical Review Letters*, 1998, **80**, 4337–4340.

54 F. W. Ostermayer and P. A. Kohl, *Applied Physics Letters*, 1981, **39**, 76–78.

55 W. E. Spicer, I. Lindau, P. Skeath and C. Y. Su, *Journal of Vacuum Science and Technology*, 1980, **17**, 1019–1027.

56 W. E. Spicer, *Journal of Vacuum Science & Technology B: Microelectronics and Nanometer Structures*, 1988, **6**, 1245.

57 L. Kornblum, D. P. Fenning, J. Faucher, J. Hwang, A. Boni, M. G. Han, M. D. Morales-Acosta, Y. Zhu, E. I. Altman, M. L. Lee, C. H. Ahn, F. J. Walker and Y. Shao-Horn, *Energy Environ. Sci.*, 2017, **10**, 377–382.

58 Y. Wu, M. K. Y. Chan and G. Ceder, *Phys. Rev. B*, 2011, **83**, 235301.

59 W. H. Laflere, F. Cardon and W. P. Gomes, *Surface Science*, 1974, **44**, 541–552.

60 D. Mandler and A. J. Bard, *Langmuir*, 1990, **6**, 1489–1494.

61 W. A. Smith, I. D. Sharp, N. C. Strandwitz and J. Bisquert, *Energy & Environmental Science*, 2015, **8**, 2851–2862.

62 P. Allongue, S. Blonkowski and E. Souteyrand, *Electrochimica Acta*, 1992, **37**, 781–797.

63 X. Li, *Current Opinion in Solid State and Materials Science*, 2012, **16**, 71–81.

64 X. Li and P. W. Bohn, *Appl. Phys. Lett.*, 2000, **77**, 2572–2574.

65 Z. Huang, N. Geyer, P. Werner, J. de Boor and U. Gösele, *Adv. Mater.*, 2011, **23**, 285–308.